



## Extreme Reconfigurable Nanoelectronics at the $\text{CaZrO}_3/\text{SrTiO}_3$ Interface

Chen, Lu; Li, Jianan; Tang, Yuhe; Pai, Yun-Yi; Chen, Yunzhong; Pryds, Nini; Irvin, Patrick; Levy, Jeremy

*Published in:*  
Advanced Materials

*Link to article, DOI:*  
[10.1002/adma.201801794](https://doi.org/10.1002/adma.201801794)

*Publication date:*  
2018

*Document Version*  
Peer reviewed version

[Link back to DTU Orbit](#)

*Citation (APA):*  
Chen, L., Li, J., Tang, Y., Pai, Y.-Y., Chen, Y., Pryds, N., Irvin, P., & Levy, J. (2018). Extreme Reconfigurable Nanoelectronics at the  $\text{CaZrO}_3/\text{SrTiO}_3$  Interface. *Advanced Materials*, 30(33), Article 1801794. <https://doi.org/10.1002/adma.201801794>

---

### General rights

Copyright and moral rights for the publications made accessible in the public portal are retained by the authors and/or other copyright owners and it is a condition of accessing publications that users recognise and abide by the legal requirements associated with these rights.

- Users may download and print one copy of any publication from the public portal for the purpose of private study or research.
- You may not further distribute the material or use it for any profit-making activity or commercial gain
- You may freely distribute the URL identifying the publication in the public portal

If you believe that this document breaches copyright please contact us providing details, and we will remove access to the work immediately and investigate your claim.

# Extreme Reconfigurable Nanoelectronics at the CaZrO<sub>3</sub>/SrTiO<sub>3</sub> Interface

*Lu Chen, Jianan Li, Yuhe Tang, Yun-Yi Pai, Yunzhong Chen, Nini Pryds, Patrick Irvin, and Jeremy Levy\**

L. Chen, J. Li, Y. Tang, Y.-Y. Pai, Dr. P. Irvin, Prof. J. Levy  
Department of Physics and Astronomy, University of Pittsburgh, Pittsburgh, PA 15260, USA  
Pittsburgh Quantum Institute, Pittsburgh, PA 15260, USA

E-mail: [jlevy@pitt.edu](mailto:jlevy@pitt.edu)

Dr. Y. Chen, Prof. N. Pryds

Department of Energy Conversion and Storage, Technical University of Denmark, Risø  
Campus, Roskilde 4000, Denmark

Keywords: complex oxides, two-dimensional electron system, c-AFM lithography, superconductivity, quantum transport

Complex oxide heterostructures exhibit diverse emergent properties, including a tunable metal-insulator transition,<sup>[1]</sup> magnetism,<sup>[2]</sup> superconductivity,<sup>[3]</sup> and spin-orbit coupling.<sup>[4-5]</sup> The ability to create and reconfigure nanoscale conducting regions at the polar/non-polar LaAlO<sub>3</sub>/SrTiO<sub>3</sub> (LAO/STO) interface using the conductive atomic force microscopy (c-AFM) lithography technique has made LAO/STO an attractive platform for both studying the fundamental physics of correlated electronic systems and developing future oxide-based nanoelectronic devices. Various nanostructures have since been realized in the LAO/STO system, including sketched single-electron transistors,<sup>[6]</sup> ballistic electron waveguides,<sup>[7]</sup> field-effect transistors,<sup>[8]</sup> photodetectors,<sup>[9]</sup> and broadband THz sources and detectors.<sup>[10]</sup> But to date, few devices created by AFM lithography have been reported<sup>[11]</sup> outside of the LAO/STO system.

A two-dimensional electron system (2DES) can also be formed at the non-polar/non-polar oxide interface of CaZrO<sub>3</sub>/SrTiO<sub>3</sub> (CZO/STO) by strain-induced polarization when the CZO layer is more than the critical thickness.<sup>[12-14]</sup> Here we report extreme nanoscale control of the non-polar CZO/STO interface at room temperature using c-AFM lithography (**Figure 1a**). Conductive structures are stable with feature sizes as small as 1.2 nm at room temperature. A

variety of nanodevices are created and characterized at low temperature, providing insight into the electronic confinement of the CZO/STO interface. The ability to create nanostructures at the non-polar CZO/STO interface with the same c-AFM lithography technique expands the class of heterostructures which can be controlled at extreme nanoscale dimensions.

High quality (001) CZO film is grown on top of (001) TiO<sub>2</sub>-terminated STO substrate by pulsed laser deposition (PLD) in a two-dimensional (2D) layer by layer growth mode. A thickness of the CZO is chosen to be close to the metal-insulator transition (8 unit cells), and the film thickness is monitored during growth by counting the intensity oscillations of the reflection high-energy electron diffraction (RHEED) pattern measured in situ. Details of the growth conditions are reported elsewhere.<sup>[12]</sup> Terraces can clearly be seen from the atomic force microscopy (AFM) topography scan image (Figure 1b), confirming the CZO film is atomically smooth. Electric contact to the CZO/STO interface is fabricated by Ar<sup>+</sup> etching (25 nm) followed by sputter deposition of Ti/Au (5 nm/20 nm); a second layer of Ti/Au on top of CZO is added for wire bonding (see Experimental Section for details). The interface is found to be highly insulating (>0.5 GOhm between nearby electrodes which are separated by 2 μm) after sample processing.

The c-AFM lithography set up is shown in Figure 1a. Nanoscale conducting regions are created by applying a positive voltage (+20 V) on the AFM tip while scanning the tip in contact mode along a designed path. A sharp conductance jump can be observed once the path is complete (Figure 1c), indicating that a conducting channel has been formed at the interface. The positive threshold voltage for forming conducting channels is around +6 V. This process is reversible: when the AFM tip is biased with a negative voltage (-20 V) and moved across the existing wire, a steep drop in the conductance is observed (Figure 1c inset). **The AFM topography image after c-AFM lithography shows no visible deformation of the sample surface, even after repeated write/erase cycles.** The width of the conducting channel can be extracted by fitting the drop in the conductance to a function of the form  $G(x) = c_0 + c_1x + c_2 \tanh(x/h) +$

$c_3 x \tanh(x/h)^{[15]}$  (where  $c_{0-3}$  are fitting coefficients,  $x$  is the tip position, and  $h$  is the cutting length) and calculating the full-width at half-maximum of the corresponding differential conductance  $dG/dx$ . The wire width extracted in the inset of Figure 1c is around 2.8 nm. As shown in Figure 1d, when the tip bias voltage decreases from 20 V to 10 V, the nanowire width at the CZO/STO interface decreases to 1.2 nm. The nanowires created at the CZO/STO interface remain extremely narrow at all writing voltages tested, in contrast to nanowires formed at the LAO/STO interface, where the wire width depends sensitively on the writing voltage.<sup>[15]</sup> Compared to nanowires defined by conventional lithographic processes, ultrathin conducting regions created by c-AFM lithography are electrostatically confined which have much smoother confinement profiles, and are physically separated from the surface charges that define their shape thus are less susceptible to atomic-scale defects.<sup>[16]</sup> Such high quality and highly reconfigurable nanostructures, with dimensions comparable to most single-walled carbon nanotubes, hold great promise for alternative oxide-based nanoelectronics with length scales beyond the current semiconductor technology node, as well as offer new opportunities to study novel physics in CZO/STO heterostructures.

The ability to achieve a metal-insulator transition locally and reversibly by the same c-AFM lithography technique at a non-polar/non-polar interface naturally raises the question of the physical mechanisms responsible for the formation and suppression of conducting channels at complex oxide interfaces. To narrow down the possible physical mechanisms at play in the writing and erasing process, we compare the writing in air and under modest vacuum, as shown in Figure 1e. Before each writing, the sample is raster-scanned with a negative voltage to remove any remaining conducting patterns. The four-terminal conductance shows a well-defined jump (red line) when writing in air with a relative humidity around 43% at 22 °C. After erasing the existing nanowire, the AFM chamber is evacuated to a pressure of  $3.9 \times 10^{-1}$  mbar. The same four-terminal structure is then written with identical writing parameters, but no conductance jump is observed under this modest vacuum (blue line). A subsequent writing is

repeated after re-exposing the sample to air and a four-terminal conductance jump is again observed. The inability to write under vacuum is consistent with the same H<sub>2</sub>O-mediated surface protonation process as with the LAO/STO system.<sup>[17-18]</sup> LAO/STO has a critical thickness of 4 unit cells,<sup>[1]</sup> and 3-unit-cell LAO/STO can be hysteretically switched between conductive and insulating states either by application of +/-100V<sup>[1]</sup> or by c-AFM lithography.<sup>[15]</sup> For this system, the polarization of the LAO layer brings the interface close to the metal-insulator transition. Application of strain (e.g., from LSAT substrate<sup>[19]</sup>) can shift the critical thickness due to strain-induced polarizations. The CZO layer is non-polar, but is not lattice matched with the STO substrate. In this case, the polarization discontinuity arises solely due to strain-induced effects. When the strain-induced polarization is close to the metal-insulator transition, the interface can then be switched between conducting and insulating state through surface protonation arising from c-AFM lithography. Such a process allows numerous writing and erasing cycles without degradation of the oxide heterostructures, confirmed by repeated writing and erasing in the same region. The narrower nanostructures created at the CZO/STO interface may also be explained by variations in surface chemistry that result in a smaller water meniscus size formed under the AFM tip on CZO surface compared to LAO. Further insight into the writing and erasing mechanism could come from a more comprehensive study with different atmospheric conditions or surface adsorbates. For example, experiments similar to Ref. 18 could be used to gauge whether protons are the primary ionic species.

At low temperatures, the electronic widths are expected to greatly increase<sup>[20-21]</sup> due to the increase in dielectric permittivity of STO from 300 at room temperature to over 20,000 at low temperatures<sup>[22]</sup>. To investigate the low-temperature electronic properties of CZO/STO nanostructures, we focus on three types of devices, all created within the same 20  $\mu\text{m}$   $\times$  20  $\mu\text{m}$  region (“canvas”). Before writing each device, the canvas is restored to a fully insulating phase by raster-scanning the entire canvas with a negative voltage, both vertically and horizontally at high resolution (5 nm spacing). Transport properties of a conducting nanowire at the CZO/STO

interface are explored by writing a 5  $\mu\text{m}$ -long nanowire device, as shown in **Figure 2a**. A T-shaped side gate, located 1.1  $\mu\text{m}$  away from the main channel, acts to adjust the chemical potential of the nanowire. Magnetotransport measurements are taken in a dilution refrigerator with a superconducting magnet whose axis is oriented out-of-plane with respect to the sample surface. Four-terminal current-voltage ( $I$ - $V$ ) curves are acquired by sourcing voltage from electrode 7, measuring current  $I_{73}$  from electrode 3, and measuring the voltage  $V_{15}$  across electrodes 1 and 5. The upper panel of the Figure 2b shows the average of ten  $I$ - $V$  curves, acquired at  $T = 50$  mK and  $B = 0$  T. A flat region is observed for small current values. The bottom of Figure 2b is the differential resistance  $dV/dI$  calculated from the averaged  $I$ - $V$  curve in units of the resistance quantum ( $h/e^2$ ), where  $e$  is the electron charge and  $h$  is Planck's constant. A superconducting state is observed, with zero resistance within the resolution of the measurement. We define the critical current  $I_C$  as the averaged current position of the two differential resistance peaks, i.e.  $I_C = (|I^+| + |I^-|)/2$ . In this device,  $I_C = 0.9$  nA. In the superconducting state ( $|I| < I_C$ ), there is a finite resistance that increases with current, which may be attributed to thermally activated phase slips<sup>[23]</sup> or Joule heating.<sup>[24-25]</sup>

The superconducting state disappears at elevated temperatures or higher magnetic fields. Figure 2c shows the differential resistance calculated from  $I$ - $V$  curves acquired at 50 mK and under different magnetic fields from 0 T to 0.5 T with 0.005 T steps. Each curve is shifted by 0.1  $h/e^2$  for clarity. We denote the lowest differential resistance in the superconducting state ( $|I| < I_C$ ) to be  $R_S$  and the differential resistance in the normal state ( $|I| \gg I_C$ ) to be  $R_N$ . As the magnetic field increases through the superconducting transition,  $I_C$  gradually decreases while  $R_S$  and  $R_N$  both increase. Figure 2d shows an intensity map of the differential resistance as a function of magnetic field and bias current. The signal is symmetric and repeatable when reversing the direction of the magnetic field. There is an asymmetry with respect to bias current, which will be discussed below. Similarly, Figure 2e shows the differential resistance calculated from  $I$ - $V$  curves measured at zero magnetic field while stepping the temperature from 50 mK

to 500 mK in steps of 4 mK. A broad transition from the superconducting state to the normal state is observed, which is usually explained by thermally activated phase slips as reported in other superconducting nanowires.<sup>[23]</sup> A complete phase diagram of  $R_S$  as a function of both temperature and magnetic field is shown in Figure 2f. Here we define the critical temperature  $T_C$  (field  $B_C$ ) as the temperature (field) at which the differential resistance is half of  $R_N$ , yielding  $T_C = 270$  mK and  $B_C = 0.26$  T. The critical temperature and critical magnetic field observed for this system are consistent with superconductivity that originates primarily in the STO substrate.<sup>[26]</sup>

This superconducting state can also be tuned by applied gate voltages, as shown in **Figure 3**.  $I$ - $V$  curves are measured at 50 mK and zero magnetic field with different gate voltages applied to the back of the STO substrate. When sweeping the backgate voltage from 0.28 V to 2.18 V, the superconducting resistance  $R_S$  increases slightly, while the normal resistance  $R_N$  decreases by almost a factor of two (Figure 3b). The critical current  $I_C$  also increases with  $V_{bg}$  and saturates above  $V_{bg} = 1.3$  V (Figure 3c). The gate-dependent resistance modulation in both the normal ( $R_N$ ) and superconducting state ( $R_S$  and  $I_C$ ) is consistent with a superconducting gap that depends non-monotonically with carrier concentration.<sup>[27]</sup> Note that the narrow width of the nanowires produces significant electric flux focusing, so a relatively small backgate voltage is sufficient to tune the carrier concentration in the thin nanowires.<sup>[28]</sup> The  $I$ - $V$  curves exhibit hysteresis that increases with increasing  $V_{bg}$ , which has been attributed to motion of ferroelastic domains.<sup>[29]</sup> The asymmetry in the differential resistance intensity map (Figure 2d) provides additional evidence of this hysteretic behavior, where we only measured the  $I$ - $V$  curves in one direction. Similar gate-dependent resistance modulation in both the normal and superconducting state can also be observed when tuning the device with a sidegate (Figure 3d-e), except the critical current  $I_C$  continues to increase even at the largest sidegate voltage tested (100 mV) (Figure 3f). Further tuning of the superconductivity might be available by increasing the sidegate voltage range.

Properties of two-dimensional CZO/STO channels are investigated by writing a Hall bar structure (**Figure 4**) with channel width  $w = 0.5 \mu\text{m}$  and length  $L = 3 \mu\text{m}$ . This pattern is created by raster-scanning the c-AFM tip within the designed rectangular regions in both horizontal and vertical directions with a line spacing of 10 nm. The longitudinal Hall resistance  $R_{xx}$  (transverse Hall resistance  $R_{xy}$ ) is measured as a function of magnetic field at 50 mK by sourcing voltage from electrode 1, measuring current from electrode 3 and measuring  $V_{xx}$  ( $V_{xy}$ ) from electrode 2 (7) and electrode 5 (2). The mobility  $\mu_{\text{Hall}}$  and the carrier density  $n_{\text{Hall}}$  extracted from the Hall measurement are  $3,600 \text{ cm}^2\text{V}^{-1}\text{s}^{-1}$  and  $2.47 \times 10^{13} \text{ cm}^{-2}$ , respectively. The  $n_{\text{Hall}}$  is comparable to other STO-based oxide heterostructures, while the  $\mu_{\text{Hall}}$  is relatively high.<sup>[30-35]</sup>  $R_{xx}$  shows a large positive magnetoresistance and oscillations at higher magnetic fields, which are more obvious after subtraction of a smooth background and plotted as a function of  $1/B$  (Figure 4c). Such oscillations resemble the Shubnikov-de Haas (SdH) effect, despite the modest mobility and high carrier density. A fast Fourier transform (FFT) shows a broad peak around 30.6 T, corresponding to a carrier density of  $n_{\text{SdH}} = 1.48 \times 10^{12} \text{ cm}^{-2}$ . The discrepancy of carrier densities obtained from low field Hall measurement and high field SdH oscillations have been widely reported in other STO-based 2D devices,<sup>[36-40]</sup> and recently it has been attributed to the naturally formed quasi-1D ferroelastic domain boundaries in these 2D systems, where the magnetic field depopulates the energy subbands.<sup>[21]</sup> Quantum oscillations are also observed in  $R_{xy}$ . The measured  $R_{xy}$  shows slight deviation from anti-symmetry for positive and negative magnetic fields, and an offset at zero field, which can be attributed to the mixing of  $R_{xx}$  and  $R_{xy}$ , and is likely enhanced by naturally occurring ferroelastic domain structure within the Hall bar channel.<sup>[41]</sup>

To further characterize the electronic confinement of the interfacial nanostructures, a more complicated waveguide device that consists of two highly transparent barriers has also been written and characterized (**Figure 5a**). The barriers are 5 nm wide and separated by 50 nm and the total length of the main channel is 500 nm. This device is created in two steps. First a

positive voltage (+20 V) is applied to the AFM tip to write the main channel, then the tip is biased with a small positive voltage (+5 V) and moved along the same writing path, during which two negative voltage pulses (-11 V) are applied to create the two narrow barriers. The chemical potential  $\mu$  of the nanowire segment between the two barriers is tuned by a sidegate that is located 800 nm away from the main channel. Zero-bias four-terminal conductance  $G = dI/dV$  is measured as a function of sidegate voltages at 50 mK and under different magnetic fields (Figure 5b). At large negative sidegate voltages, the waveguide conductance is tuned to zero. As the sidegate voltage is increased, the four-terminal conductance increases to more than  $5 e^2/h$  (conductance quantum) at 0 T (red line). Signatures associated with the superconducting regime appear as sharp increases in conductance. Such sharp increases disappear for magnetic fields  $|B| > 0.26$  T (green line). The remaining additional features may be attributed to either quantum mechanical tunneling through the barriers, scattering due to impurities in the waveguide, or both. For an ideal coherent quantum waveguide, each spin-resolved energy subband contributes one conductance quantum ( $e^2/h$ ) to the total conductance.<sup>[20]</sup> At 9 T, clear quantized plateaus near 1, 2, 3, and 4  $e^2/h$  are resolved (blue line). However, the conductance steps are not precisely quantized at integer values of  $e^2/h$ . Nonetheless the ability to tune the device to the lowest spin-resolved conductance plateau ( $\cong e^2/h$ ) is a good indication that quasi-ballistic transport can be achieved in the waveguide created at the CZO/STO interface. The electronic width at low temperatures, while larger than the room-temperature width, is still significantly smaller than the measured scattering length.

The transconductance  $dG/d\mu$  is calculated by taking derivative of the conductance curves with respect to the chemical potential  $\mu$  (Figure 5c), revealing transitions where each new subband contributes to transport. The chemical potential  $\mu$  is converted from  $V_{sg}$  by the lever-arm  $\alpha$ , which can be extracted from the finite-bias spectroscopy measurement.<sup>[20]</sup>  $I$ - $V$  curves are taken under different sidegate voltages at 9 T and 50 mK. Figure S1 shows the corresponding transconductance map calculated by taking the derivative of  $dI/dV$  with respect to  $V_{sg}$ . Lever-

arm  $\alpha = e\Delta V_{sd}/\Delta V_{sg}$ , where the source-drain voltage difference  $\Delta V_{sd}$  and sidegate voltage difference  $\Delta V_{sg}$  mark the same transition between adjacent subbands.  $\alpha$  extracted here is around  $12.2 \mu\text{eV/mV}$ , which gives a Landé  $g$ -factor  $g = e\Delta V_{sd}/\mu_B B \approx 0.5$  ( $\mu_B$  is the Bohr magneton). As mentioned above, signatures associated with the superconducting regime are observed near zero magnetic field and disappear at higher magnetic fields. The lowest two spin-resolved subbands are split with an offset  $B_p \sim 0.6$  T (Figure 5d), signifying residual electron pairing outside of the superconducting regime.<sup>[42]</sup> Pairing field ( $B_p$ ) can be extracted from the intercepts of the linear fits for both positive (0.57 T) and negative (-0.72 T) magnetic fields, and are larger than the upper critical magnetic field for superconductivity in this system (0.26 T). Such electron pairing without superconductivity has been reported in LAO/STO, where attractive electron-electron interactions are believed to suppress back-scattering from impurities and lead to electron pairing without superconductivity.<sup>[42]</sup> **The attractive electron-electron interaction is also believed to be responsible for the increased mobility in the nanowires created by c-AFM lithography at the LAO/STO interface when the channel width is reduced below 100 nm.**<sup>[16]</sup> The transconductance is also measured at  $T = 500$  mK and  $T = 900$  mK (Figure S2b-c), and we observe the same splitting even at 900 mK, which is far above the transition temperature for superconductivity (270 mK). It is also interesting to note that the electron pairing field appears to increase with increasing temperature, reaching  $B_p = 3$  T at  $T = 900$  mK (Figure S2d-f), in contrast to what has been observed in LAO/STO. Further experiments, such as characterization of the temperature dependence of  $g$ -factor, are needed to understand the physical mechanism responsible for this increase.

The ability to create arbitrary conducting nanostructures that can access quasi-1D, 2D, and local electronic properties of the complex oxide interface enables a new pathway to study fundamental questions of low-dimensional systems. Here we have shown that c-AFM lithography can control the metal-insulator transition at the non-polar  $\text{CaZrO}_3/\text{SrTiO}_3$  interface,

despite the lack of intrinsic polar discontinuity at the interface. The mechanism for writing/erasing has been attributed to a similar surface protonation/deprotonation process as in the  $\text{LaAlO}_3/\text{SrTiO}_3$  system. Nanoscale conducting regions appear to be extremely narrow at room temperature. Nanodevices such as nanowires, Hall bars, and waveguides are created, through which tunable superconductivity, quantum oscillations, electron pairing outside the superconducting regime, and quasi-ballistic transport properties of the CZO/STO interface have been characterized. The success with extreme nanoscale control over the metal-insulator transition at the non-polar  $\text{CaZrO}_3/\text{SrTiO}_3$  interface opens up new opportunities both for fundamental research and future oxide-based nanoelectronics.

### **Experimental Section**

*Sample patterning.*  $\text{CaZrO}_3/\text{SrTiO}_3$  devices are patterned with standard photolithography using AZ4210 photoresist. The interface of  $\text{CaZrO}_3/\text{SrTiO}_3$  is etched with an argon ion mill (Commonwealth Scientific Ion Mill) at 500 W and 10 mA for 25 minutes. Electrodes contacting the interface are formed by filling the etched trenches with 4 nm of titanium and 25 nm of gold using a Perkin Elmer 6J sputtering system. Excessive metals are lifted off in Microposit Remover 1165 at 50°C for 18 hours. Bonding pads are sputtered onto the top surface with 4 nm titanium and 50 nm gold. The sample is finally cleaned in acetone and isopropyl alcohol with an ultrasonic cleaner, followed by oxygen plasma using an IPC Barrel Etcher, before measurement.

*c-AFM lithography.* The conductive atomic force microscope lithography is performed using an Asylum Research MFP-3D AFM. The DC writing voltage is applied to the c-AFM tip (highly doped silicon) through a 1 G $\Omega$  series resistor. The interface of  $\text{CaZrO}_3/\text{SrTiO}_3$  is grounded during writing. All the devices are written under ambient condition unless otherwise specified, with a typical relative humidity around 35% and temperature of 27°C. The

comparison of writing in air and under vacuum is performed in a customized Nanomagnetics Instruments LT-AFM.

*Characterization.* Low temperature transport measurements are carried out in a Quantum Design PPMS dilution refrigerator. Source voltages are applied by a 24-bit digital/analog converters (National Instruments PXI-4461), which can also simultaneously perform 24-bit analog/digital conversion. The drain current is measured after amplified by a sub-femto-ampere current amplifier (Femto DDPCA-300). The four-terminal voltage drop is measured by a 1 T $\Omega$  input impedance true differential voltage amplifier (Femto DLPVA). Zero-bias conductance measurements for the waveguide device are taken by sourcing small AC voltages (50  $\mu$ V) with zero DC offset and recording the demodulated drain current and four-terminal voltage drop.

## Supporting Information

Supporting Information is available from the Wiley Online Library or from the author.

## Acknowledgements

J. Levy acknowledges support from the Vannevar Bush Faculty Fellowship program sponsored by the Basic Research Office of the Assistant Secretary of Defense for Research and Engineering and funded by the Office of Naval Research through grant N00014-15-1-2847.

Received: ((will be filled in by the editorial staff))

Revised: ((will be filled in by the editorial staff))

Published online: ((will be filled in by the editorial staff))

## References

- [1] S. Thiel, G. Hammerl, A. Schmehl, C. W. Schneider, J. Mannhart, *Science* **2006**, *313*, 1942.
- [2] A. Brinkman, M. Huijben, M. van Zalk, J. Huijben, U. Zeitler, J. C. Maan, W. G. van der Wiel, G. Rijnders, D. H. A. Blank, H. Hilgenkamp, *Nat. Mater.* **2007**, *6*, 493.
- [3] A. D. Caviglia, S. Gariglio, N. Reyren, D. Jaccard, T. Schneider, M. Gabay, S. Thiel, G. Hammerl, J. Mannhart, J. M. Triscone, *Nature* **2008**, *456*, 624.
- [4] A. D. Caviglia, M. Gabay, S. Gariglio, N. Reyren, C. Cancellieri, J. M. Triscone, *Phys. Rev. Lett.* **2010**, *104*, 126803.
- [5] M. Ben Shalom, M. Sachs, D. Rakhmilevitch, A. Palevski, Y. Dagan, *Phys. Rev. Lett.* **2010**, *104*, 126802.
- [6] G. Cheng, P. F. Siles, F. Bi, C. Cen, D. F. Bogorin, C. W. Bark, C. M. Folkman, J.-W. Park, C.-B. Eom, G. Medeiros-Ribeiro, J. Levy, *Nat. Nanotechnol.* **2011**, *6*, 343.
- [7] M. Tomczyk, G. Cheng, H. Lee, S. Lu, A. Annadi, J. P. Veazey, M. Huang, P. Irvin, S. Ryu, C.-B. Eom, J. Levy, *Phys. Rev. Lett.* **2016**, *117*, 096801.
- [8] C. Cen, S. Thiel, J. Mannhart, J. Levy, *Science* **2009**, *323*, 1026.
- [9] P. Irvin, Y. Ma, D. F. Bogorin, C. Cen, C. W. Bark, C. M. Folkman, C.-B. Eom, J. Levy, *Nat. Photonics* **2010**, *4*, 849.

- [10] Y. Ma, M. Huang, S. Ryu, C. W. Bark, C.-B. Eom, P. Irvin, J. Levy, *Nano Lett.* **2013**, *13*, 2884.
- [11] D. V. Christensen, M. von Soosten, F. Trier, T. S. Jespersen, A. Smith, Y. Chen, N. Pryds, *Adv. Electron. Mater.* **2017**, *3*, 1700026.
- [12] Y. Chen, F. Trier, T. Kasama, D. V. Christensen, N. Bovet, Z. I. Balogh, H. Li, K. T. S. Thydén, W. Zhang, S. Yazdi, P. Norby, N. Pryds, S. Linderoth, *Nano Lett.* **2015**, *15*, 1849.
- [13] S. Nazir, J. Cheng, K. Yang, *ACS Appl. Mater. Interfaces* **2016**, *8*, 390.
- [14] J. Cheng, S. Nazir, K. Yang, *ACS Appl. Mater. Interfaces* **2016**, *8*, 31959.
- [15] C. Cen, S. Thiel, G. Hammerl, C. W. Schneider, K. E. Andersen, C. S. Hellberg, J. Mannhart, J. Levy, *Nat. Mater.* **2008**, *7*, 298.
- [16] P. Irvin, J. P. Veazey, G. Cheng, S. Lu, C.-W. Bark, S. Ryu, C.-B. Eom, J. Levy, *Nano Lett.* **2013**, *13*, 364.
- [17] F. Bi, D. F. Bogorin, C. Cen, C. W. Bark, J.-W. Park, C.-B. Eom, J. Levy, *Appl. Phys. Lett.* **2010**, *97*, 173110.
- [18] K. A. Brown, S. He, D. J. Eichelsdoerfer, M. Huang, I. Levy, H. Lee, S. Ryu, P. Irvin, J. Mendez-Arroyo, C.-B. Eom, C. A. Mirkin, J. Levy, *Nat. Commun.* **2016**, *7*, 10681.
- [19] C. W. Bark, D. A. Felker, Y. Wang, Y. Zhang, H. W. Jang, C. M. Folkman, J. W. Park, S. H. Baek, H. Zhou, D. D. Fong, X. Q. Pan, E. Y. Tsymbal, M. S. Rzechowski, C. B. Eom, *Proc. Natl. Acad. Sci. U.S.A.* **2011**, *108*, 4720.
- [20] A. Annadi, S. Lu, H. Lee, J.-W. Lee, G. Cheng, A. Tylan-Tyler, M. Briggeman, M. Tomczyk, M. Huang, D. Pekker, C.-B. Eom, P. Irvin, J. Levy, *ArXiv e-prints* **2016**, *1611*, arXiv:1611.05127.
- [21] G. Cheng, A. Annadi, S. Lu, H. Lee, J.-W. Lee, M. Huang, C.-B. Eom, P. Irvin, J. Levy, *Phys. Rev. Lett.* **2018**, *120*, 076801.
- [22] R. C. Neville, B. Hoeneisen, C. A. Mead, *J. Appl. Phys.* **1972**, *43*, 2124.

- [23] J. S. Langer, V. Ambegaokar, *Phys. Rev.* **1967**, *164*, 498.
- [24] W. J. Skocpol, M. R. Beasley, M. Tinkham, *J. Appl. Phys.* **1974**, *45*, 4054.
- [25] M. Tinkham, J. U. Free, C. N. Lau, N. Markovic, *Phys. Rev. B* **2003**, *68*, 134515.
- [26] C. S. Koonce, M. L. Cohen, J. F. Schooley, W. R. Hosler, E. R. Pfeiffer, *Phys. Rev.* **1967**, *163*, 380.
- [27] J. A. Bert, K. C. Nowack, B. Kalisky, H. Noad, J. R. Kirtley, C. Bell, H. K. Sato, M. Hosoda, Y. Hikita, H. Y. Hwang, K. A. Moler, *Phys. Rev. B* **2012**, *86*, 060503.
- [28] P. V. Joshua, C. Guanglei, I. Patrick, C. Cheng, F. B. Daniela, B. Feng, H. Mengchen, B. Chung-Wung, R. Sangwoo, C. Kwang-Hwan, E. Chang-Beom, L. Jeremy, *Nanotechnology* **2013**, *24*, 375201.
- [29] M. Honig, J. A. Sulpizio, J. Drori, A. Joshua, E. Zeldov, S. Ilani, *Nat. Mater.* **2013**, *12*, 1112.
- [30] S. Mathew, A. Annadi, T. K. Chan, T. C. Asmara, D. Zhan, X. R. Wang, S. Azimi, Z. Shen, A. Rusydi, Ariando, M. B. H. Breese, T. Venkatesan, *ACS Nano* **2013**, *7*, 10572.
- [31] C. He, T. D. Sanders, M. T. Gray, F. J. Wong, V. V. Mehta, Y. Suzuki, *Phys. Rev. B* **2012**, *86*, 081401.
- [32] A. Annadi, A. Putra, Z. Q. Liu, X. Wang, K. Gopinadhan, Z. Huang, S. Dhar, T. Venkatesan, Ariando, *Phys. Rev. B* **2012**, *86*, 085450.
- [33] C. P. Chang, J. G. Lin, H. T. Jeng, S. L. Cheng, W. F. Pong, Y. C. Shao, Y. Y. Chin, H. J. Lin, C. W. Chen, J. R. Yang, C. H. Chen, M. W. Chu, *Phys. Rev. B* **2013**, *87*, 075129.
- [34] P. Xu, W. Han, P. M. Rice, J. Jeong, M. G. Samant, K. Mohseni, H. L. Meyerheim, S. Ostanin, I. V. Maznichenko, I. Mertig, E. K. U. Gross, A. Ernst, S. S. P. Parkin, *Adv. Mater.* **2017**, *29*, 1604447.
- [35] K. Shibuya, T. Ohnishi, M. Lippmaa, M. Oshima, *Appl. Phys. Lett.* **2007**, *91*, 232106.

- [36] S. Zeng, W. Lü, Z. Huang, Z. Liu, K. Han, K. Gopinadhan, C. Li, R. Guo, W. Zhou, H. H. Ma, L. Jian, T. Venkatesan, Ariando, *ACS Nano* **2016**, *10*, 4532.
- [37] M. Yang, K. Han, O. Torresin, M. Pierre, S. Zeng, Z. Huang, T. V. Venkatesan, M. Goiran, J. M. D. Coey, Ariando, W. Escoffier, *Appl. Phys. Lett.* **2016**, *109*, 122106.
- [38] Y. Kozuka, M. Kim, C. Bell, B. G. Kim, Y. Hikita, H. Y. Hwang, *Nature* **2009**, *462*, 487.
- [39] B. Jalan, S. Stemmer, S. Mack, S. J. Allen, *Phys. Rev. B* **2010**, *82*, 081103.
- [40] Y. Matsubara, K. S. Takahashi, M. S. Bahramy, Y. Kozuka, D. Maryenko, J. Falson, A. Tsukazaki, Y. Tokura, M. Kawasaki, *Nat. Commun.* **2016**, *7*, 11631.
- [41] Y. Frenkel, N. Haham, Y. Shperber, C. Bell, Y. Xie, Z. Chen, Y. Hikita, H. Y. Hwang, B. Kalisky, *ACS Appl. Mater. Interfaces* **2016**, *8*, 12514.
- [42] G. Cheng, M. Tomczyk, S. Lu, J. P. Veazey, M. Huang, P. Irvin, S. Ryu, H. Lee, C.-B. Eom, C. S. Hellberg, J. Levy, *Nature* **2015**, *521*, 196.

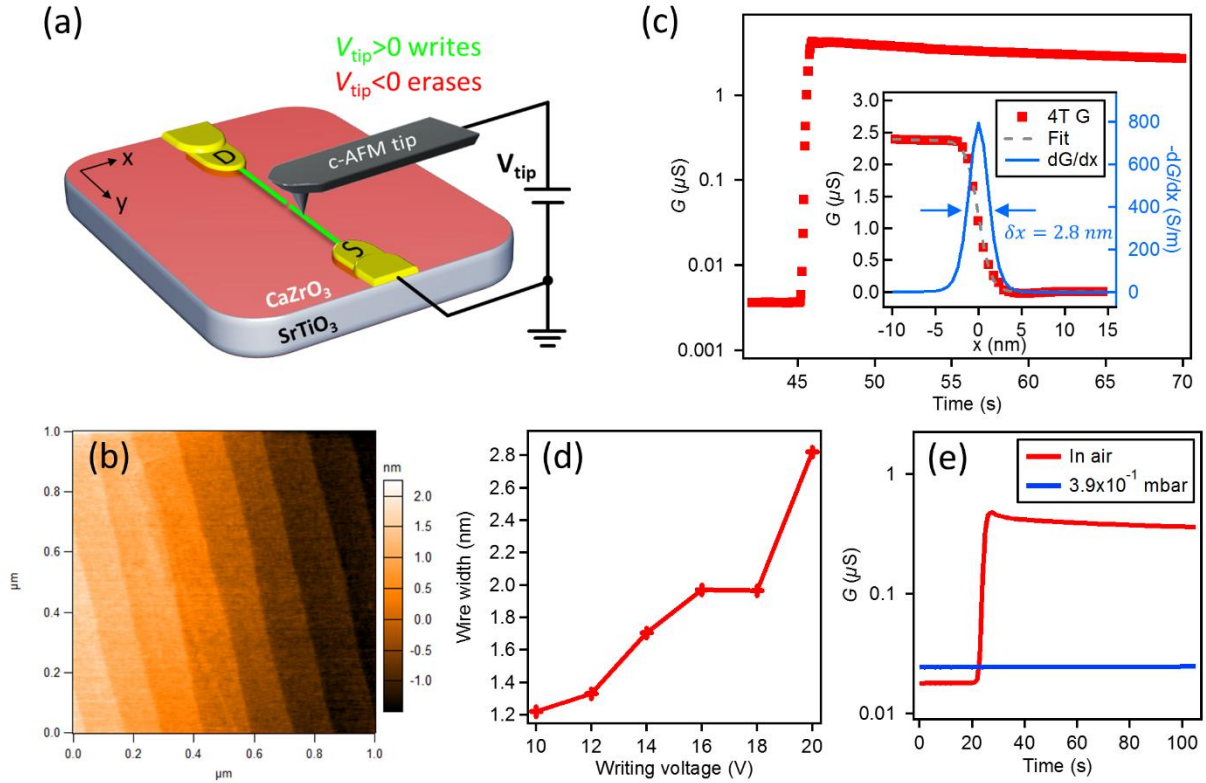


**Figure 1.** Creating and erasing nanostructures at the CaZrO<sub>3</sub>/SrTiO<sub>3</sub> (CZO/STO) interface. (a) Schematic drawing of c-AFM lithography. Gold electrodes are in direct contact with the CZO/STO interface. Green wires indicate the nanoscale conducting regions at the interface created by scanning a positively-biased AFM tip from one electrode to the other. The junction in the middle of the nanowire is formed by applying a negative voltage on the AFM tip and cutting across the nanowire. (b) AFM topography image showing an atomically smooth CZO surface. (c) The four terminal conductance increases over 3 orders of magnitude when a nanowire is written. Inset shows the steep drop in conductance once the nanowire is cut. The width of the nanowire can be extracted by fitting to the conductance drop and calculating its corresponding differential conductance  $-dG/dx$  as a function of tip position  $x$ . The full-width at half-maximum of the nanowire is 2.8 nm. (d) Nanowire width plotted as a function of writing voltage. (e) Comparison of writing in air and under modest vacuum. The nanowire here is 10 times longer than the nanowire in (c) and the conductance background comes from photoconductance residue.

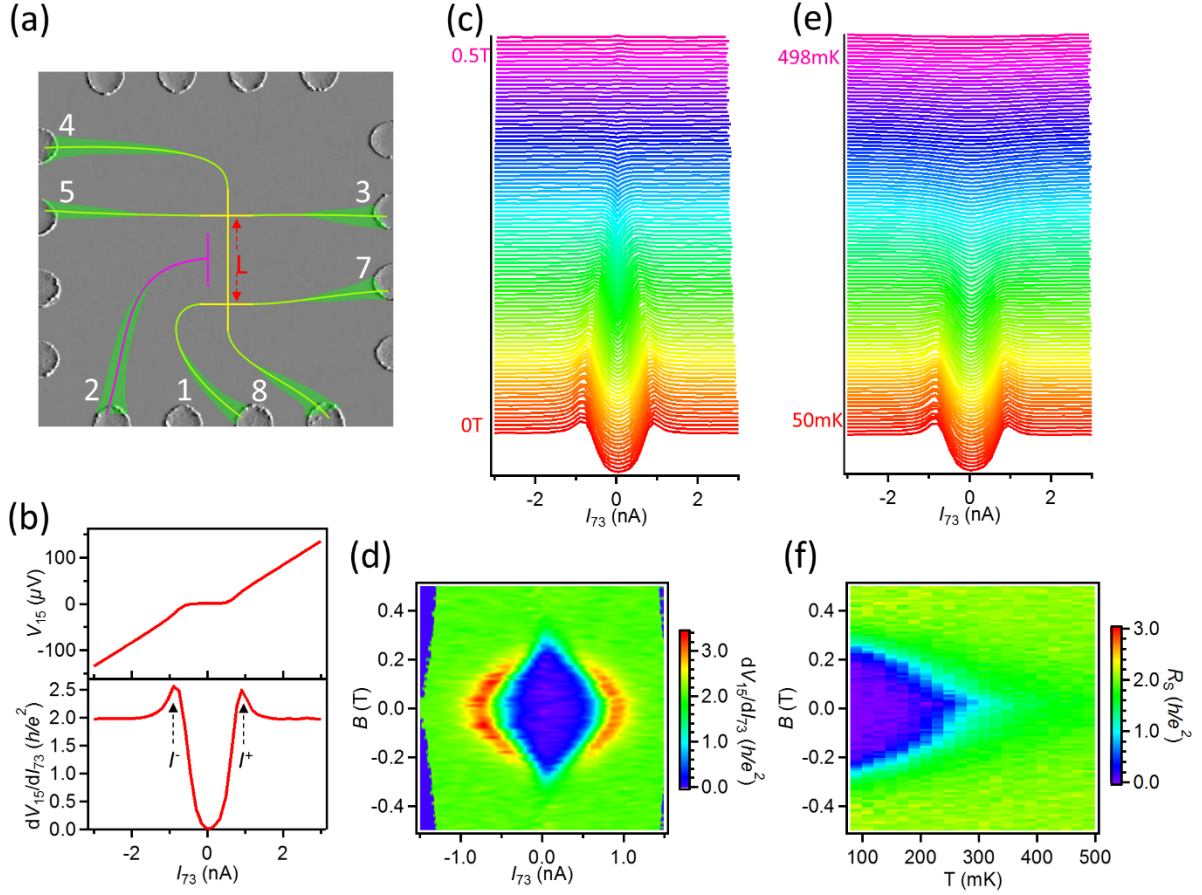


**Figure 2.** Superconductivity in a nanowire created at the  $\text{CaZrO}_3/\text{SrTiO}_3$  interface. (a) Designed c-AFM lithography pattern overlaid on an AFM topography image of the canvas. The main channel length is  $L = 5 \mu\text{m}$ . (b) The four-terminal  $I$ - $V$  curve (top) acquired at 0 T and 50 mK and the corresponding differential resistance  $dV/dI$  curve (bottom) show a superconducting state with zero resistance within the resolution of the measurement. The critical current is  $I_C = 0.9 \text{ nA}$ . (c)  $dV/dI$  curves at 50 mK with increasing out of plane magnetic field through the superconducting transition. (d)  $dV/dI$  intensity map as a function of magnetic field and bias current. (e) Temperature dependent  $dV/dI$  curves at zero magnetic field. (f) Complete temperature and field phase diagram. The normal state is restored for temperatures above 270 mK and field values above 0.26 T.

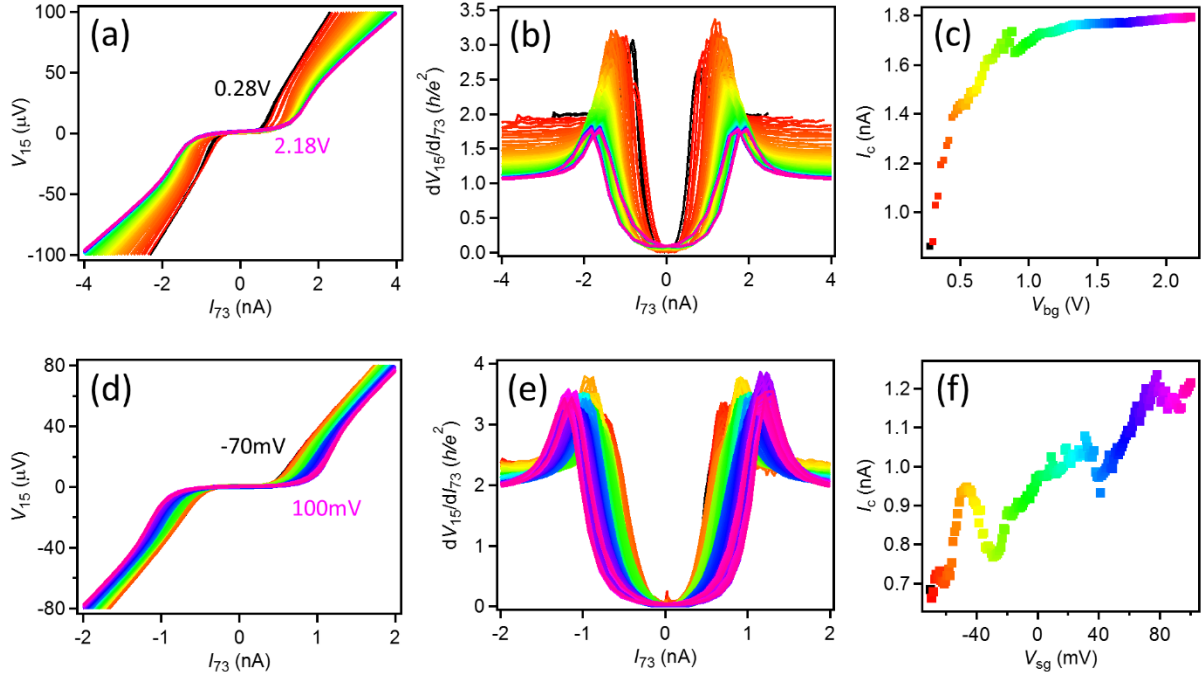


**Figure 3.** Gate tuning of superconductivity in the nanowire device. (a) and (b)  $I$ - $V$  curves and the corresponding differential resistances at different backgate voltages. (c) Critical current  $I_C$  (extracted from (b)) increases with  $V_{bg}$  and saturates above 1.3 V. (d) and (e)  $I$ - $V$  curves and the corresponding differential resistances at different sidegate voltages. (f) Critical current  $I_C$  (extracted from (e)) increases with  $V_{sg}$ .

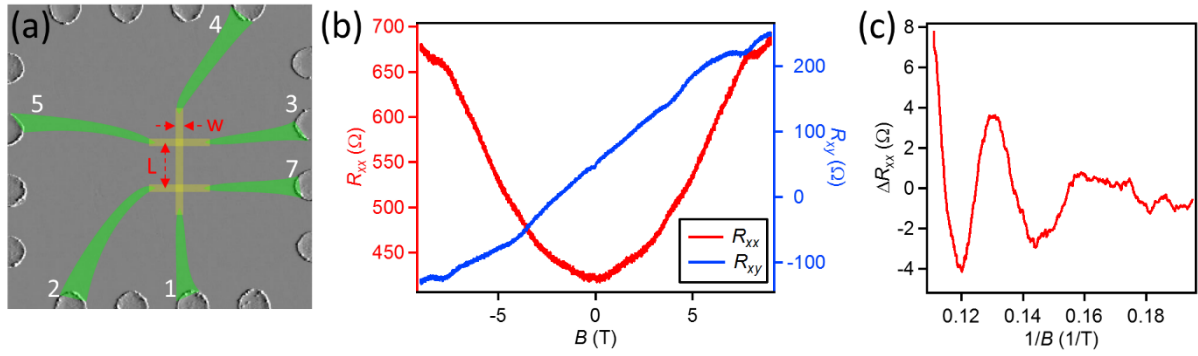


**Figure 4.** Hall bar device written at the  $\text{CaZrO}_3/\text{SrTiO}_3$  interface. (a) Designed c-AFM lithography pattern overlaid on an AFM topography image of the canvas. The width is  $w = 0.5 \mu\text{m}$  and length is  $L = 3 \mu\text{m}$ . (b)  $R_{xx}$  and  $R_{xy}$  plotted as a function of magnetic field. The mobility and the carrier density extracted from the Hall measurement are  $3,600 \text{ cm}^2\text{V}^{-1}\text{s}^{-1}$  and  $2.47 \times 10^{13} \text{ cm}^{-2}$ , respectively.  $R_{xx}$  also shows large positive magnetoresistance and quantum oscillations that resemble the SdH effect. Additional features also present in  $R_{xy}$ . (c) Oscillations in  $R_{xx}$  after subtraction of a smooth background.

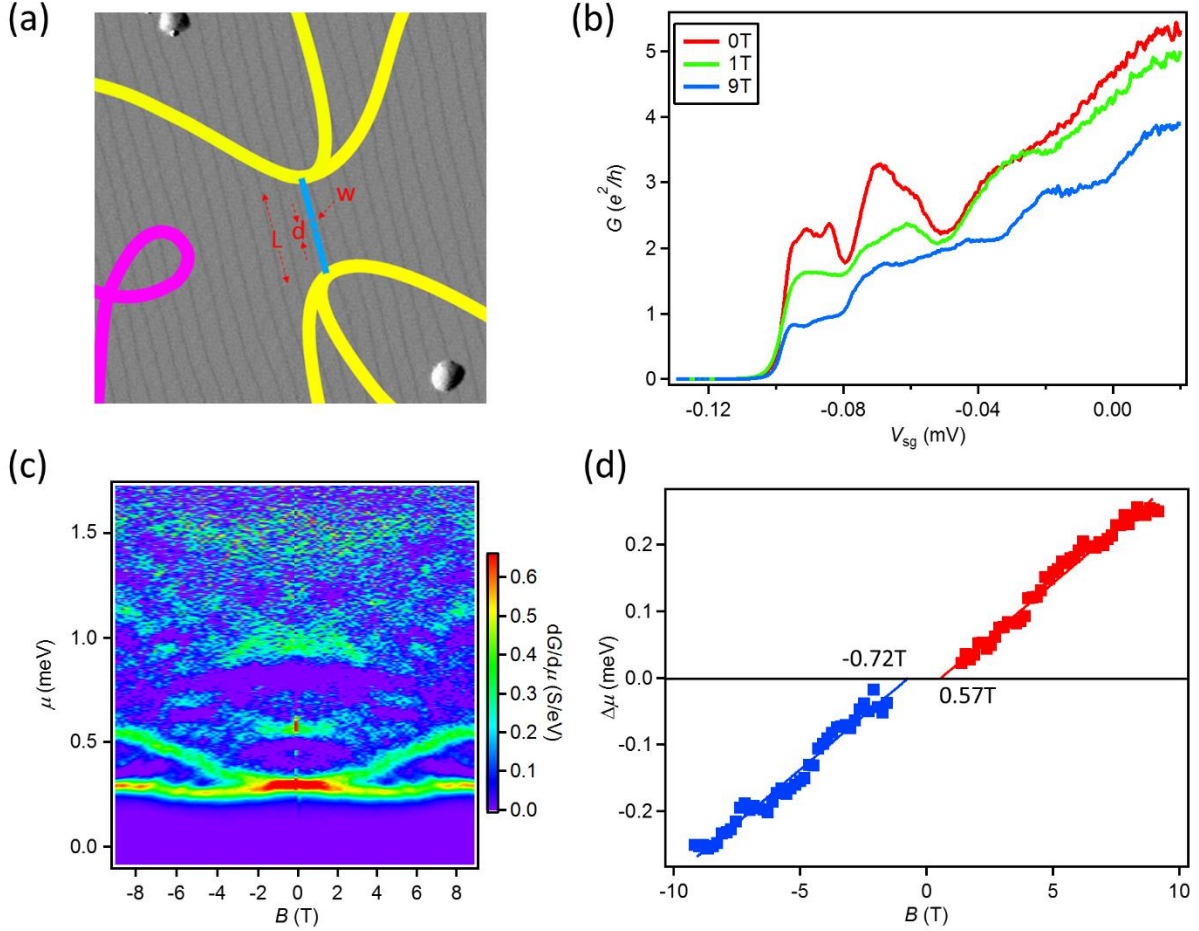


**Figure 5.** Waveguide device written at the CaZrO<sub>3</sub>/SrTiO<sub>3</sub> interface. (a) Designed c-AFM lithography pattern overlaid on an AFM topography image of the canvas. The total length of the main channel is  $L = 500$  nm, width of the barrier is  $w = 5$  nm, and separation between the two barriers is  $d = 50$  nm. (b) Zero-bias four-terminal conductance as a function of sidegate voltages at 0 T, 1 T, and 9 T. Quantized conductance plateaus develop at high magnetic fields. (c) The transconductance as a function of chemical potential  $\mu$  and magnetic field  $B$  shows peak splittings above a critical magnetic field. (d) Chemical potential difference of the split peaks as a function of magnetic field. Pairing fields can be extracted from the intercepts of the linear fit, and are larger than the upper critical magnetic field for superconductivity.

**The ToC Entry (50 – 60 words)**

**Ultra-thin (1 to 3 nm wide) nanostructures** can be realized at the non-polar  $\text{CaZrO}_3/\text{SrTiO}_3$  interface using c-AFM lithography, enabling the observation of tunable superconductivity, quantum oscillations, electron pairing without superconductivity, and quasi-ballistic transport. Such extreme nanoscale control over non-polar complex oxide interface offers new ways to investigate fundamental physics in other correlated systems and develop future oxide-based nanoelectronics.

**Keyword**

complex oxides, two-dimensional electron system, c-AFM lithography, superconductivity, quantum transport

**Authors**

Lu Chen, Jianan Li, Yuhe Tang, Yun-Yi Pai, Yunzhong Chen, Nini Pryds, Patrick Irvin, and Jeremy Levy\*

**Title**

Extreme Reconfigurable Nanoelectronics at the  $\text{CaZrO}_3/\text{SrTiO}_3$  Interface

**ToC figure**